

Contents lists available at ScienceDirect

Vacuum

journal homepage: http://www.elsevier.com/locate/vacuum





Microstructure and tribocorrosion properties of NiTi/AlNi₂Ti ternary intermetallic alloy

H. Chen*, Z. Zhang, X.H. Hao, B.X. Huang, X.C. Zhao, C.C. Hu

School of Materials Science and Engineering, Liaocheng University, Liaocheng, Shandong, 252000, China

ARTICLE INFO

Keywords:
Intermetallics
NiTi/AlNi₂Ti
Electrochemical corrosion
Tribocorrosion
Arc melting
Corrosion-wear synergistic mechanism

ABSTRACT

NiTi/AlNi $_2$ Ti intermetallic alloy consisting of AlNi $_2$ Ti primary dendrites and NiTi interdendritic phase was fabricated by arc melting process. Tribocorrosion behaviors of the alloy in 0.5 mol/L H_2SO_4 solutions were characterized using tribocorrosion tests and X-ray photoelectron spectroscopy (XPS). Corrosion-wear synergistic effect and tribocorrosion mechanism were also discussed. The tribocorrosion test results showed that the open circuit potential (OCP) of NiTi/AlNi $_2$ Ti alloy decreases and the corrosion current density increases as the sliding starts, and the decrease in the OCP value is proportional to the increase in the frictional force, indicating a strong corrosion-wear synergistic effect. The NiTi/AlNi $_2$ Ti alloy has better tribocorrosion resistance than the OCr18Ni9 material in 0.5 mol/L H_2SO_4 solution with a high OCP, low corrosion current and low wear volume. The wear volume of NiTi/AlNi $_2$ Ti alloy is about 10 times lower than that of reference material OCr18Ni9. The calculation results of materials loss (Δ V) during tribocorrosion test indicated that corrosion accelerated wear (V_{cw}) was the main corrosion-wear synergistic mechanism.

1. Introduction

Wear, corrosion and fatigue are the three most common failure modes for mechanical moving components [1,2]. Moreover, these failure modes often co-exist and interact with each other in the fields of navigation, aerospace, petrochemicals, mining, and energy, which lead to more serious material damage [3]. However, the practical application of some traditional wear-resistant materials such as cast iron, high-carbon steel and low-alloy tool steel under wear and corrosion service conditions is limited due to the lack of sufficient corrosion resistance [4]. Stainless steels are the most popular materials used in marine equipment, food and biomedical fields because of their superior mechanical properties and excellent corrosion resistance [5]. Unfortunately, the severe pitting corrosion and tribocorrosion damage of stainless steels greatly degrade their reliability and service life in marine environments [6]. Therefore, it is of great significance to develop a new material that can work under wear and corrosion conditions.

In the Al-Ni-Ti ternary system, several binary and ternary intermetallic compounds with attractive physical and mechanical properties have been subjected to increased interest in recent years [7,8]. Among those compounds, nickel-aluminum compounds are well known as high-temperature structural alloy materials, and titanium-aluminum

compounds are a class of good high-temperature corrosion resistant materials [9]. The addition of Ni is beneficial to the steady flow behavior, strain rate sensitivity and thermal deformation properties of TiAl alloy [10]. Some studies have shown that the high temperature creep resistance of Ni–Al alloy can be significantly improved by introducing Ti element into Ni–Al alloy due to the large atomic mismatch and formation of AlNi₂Ti or Al₃NiTi₂ ternary precipitation strengthening phase [11,12]. On the other hand, the introduction of the alloying element Al in the Ni–Ti binary alloy can significantly improve its mechanical properties and corrosion resistance through solid solution strengthening and precipitation of strengthening phase (TiNi or AlNi₂Ti phase) [13,14]. Therefore, ternary intermetallics in Al–Ni–Ti system are expected to have better mechanical properties and corrosion resistance than binary intermetallic alloys.

Up to now, there are four ternary intermetallic compounds identified as $Al_{13}Ni_2Ti_5$ ($\tau 1), <math display="inline">Al_2NiTi$ ($\tau 2), ~Al_3NiTi_2$ ($\tau 3) and <math display="inline">AlNi_2Ti$ ($\tau 4)$ in the Al–Ni–Ti system by thermodynamic calculation and experimental observation [15–17]. Among these compounds, L21(Heusler alloy)-Al-Ni₂Ti compound has a high melting point (1503 $^{\circ}$ C), strength and hardness, and has been extensively studied as a strengthening phase of nickel-based and iron-based superalloy [18,19]. Unfortunately, serious room-temperature brittleness and environmental brittleness are the

E-mail address: chenhui@lcu.edu.cn (H. Chen).

^{*} Corresponding author.

main obstacles that prevented the materials from industrial application as wear-resistant materials. Addition of a ductile second phase is one of the most effective means to improve the toughness of intermetallics. Moreover, in this way, it also allows us to better control on the tribological properties of the intermetallics by adjusting the trade-off between hardness and toughness, which the wear behavior of the intermetallics alloy is direct proportion to Ref. [20]. Nickel-titanium compounds such as isoatomic component NiTi exhibit a good intrinsic plasticity [21]. It is found that the strengthening phase AlNi₂Ti and the ductile NiTi can form a coherent interface AlNi₂Ti/NiTi multiphase structure, and its room temperature compression strength is as high as 2300 MPa [22]. Therefore, NiTi/AlNi₂Ti based materials are expected to have good comprehensive mechanical properties (high strength and toughness), which is similar to the traditional γ/γ' structure of nickel-based superalloys [23,24]. At the same time, the AlNi₂Ti ternary intermetallic compound has a wide composition range, its inherent high hardness and strength, good toughness and strong covalent bond atom bonding characteristics, which make it desirable to have excellent friction and wear resistance. In addition, AlNi₂Ti is expected to have excellent corrosion resistance due to its high Al, Ti content and strong covalent bond components. Research by Witkowska and Farvizi et al. showed that NiTi alloy not only has good superplasticity, but also has excellent corrosion and wear resistance [25,26]. Therefore, NiTi/Al-Ni₂Ti alloy is anticipated to be a novel wear and corrosion resistant material under harsh conditions. However, to the best of our knowledge, the current researches on NiTi/AlNi2Ti alloys are mainly focused on mechanical properties, and the researches on its corrosion, especially the tribocorrosion properties (tribocorrosion being simultaneous action of corrosion and wear) are very scarce.

Schuster and Meng et al. [16,27] studied the composition of the Al-Ni-Ti ternary system, showing that the Al element preferentially occupies the Ti site in the NiTi-Al alloy, and when the Al content is 7%-17%, the alloy is located in the NiTi-AlNi₂Ti two-phase region. And as the Al content increases, the high hardness and high strength AlNi₂Ti content of the NiTi-AlNi₂Ti alloy increases, which helps to improve the mechanical properties and wear resistance of the alloy, but results in the decrease of room temperature toughness. In this present paper, in order to obtain good mechanical properties, wear and corrosion resistance, a novel tribocorrosion resistant NiTi/AlNi2Ti intermetallic compound (composition: 13.6Al-49Ni-37.4Ti) toughened by ductile NiTi were developed and prepared by controlled atmosphere arc melting. The tribocorrosion performance was investigated by tribocorrosion testing in 0.5 mol/L H₂SO₄ solutions. In order to clarify the synergistic failure mechanism of the alloy under wear and corrosion environment, the effects of wear and corrosion interaction on tribocorrosion properties are also discussed.

2. Experimental procedure

Pure aluminum (99.8%), nickel (99.9%) and titanium (99.9%) elemental powders with an average particle size ranging from 40 to 100 µm were selected as raw materials. The mixed powders with stoichiometric composition (at. %) of 13.6Al49Ni-37.4Ti were milled for 4 h in a stainless steel vacuum jar by a planetary ball mill with a ball-to-powder ratio of 10:1 and the speed of 250 r/min. The milled powders were compacted into a disk with a diameter of 15 mm at room temperature under a pressure of 300 MPa. NiTi/AlNi₂Ti alloy was synthesized by controlled atmosphere arc melting. Before arc melting the disk was placed in a water-copper crucible in the arc melting furnace. The Mechanical and molecular pumps were used to make vacuum levels down to 4 \times $10^{-3}\mbox{ Pa.}$ Then, high purity argon of 0.5 atm was filled as the protective gas. The arc current was set to 250 A. The current was adjusted to 10 A for electromagnetic stirring when the alloy melted. Each ingot was re-melted five times and the ingot was flipped before each re-melting to ensure the homogeneity of the alloy composition. The cast ingots were cut into 10 mm \times 10 mm \times 5 mm specimens using

electro-discharge machining (EDM) for microstructure analysis and tribocorrosion tests.

The phase composition of the samples were investigated by means of X-ray diffraction (XRD, D/Dmax-2400, Rigaku, Japan) with Cu Kα radiation ($\lambda = 0.15418$ nm). All XRD experiments were performed with the diffraction angle measurement ranged from 20 to 90° , step size 0.02° and scanning rate of 0.1°/s. Prior to microstructural analysis, the samples were mechanically polished and then chemically etched with saturated FeCl3 and HCl solutions for 20-30 s. Microstructure of the alloy ingots was characterized by Field-emission scanning electron microscopy (FESEM, JSM-6700F, JEOL, Japan) equipped with an energy dispersive spectroscopy (EDS). The SEM and EDS were also performed in vacuum. The volume fraction of AlNi2Ti phase was measured by quantitative metallographic analysis using commercial image analysis software on high-contrast SEM photographs (500 magnifications). The hardness of the alloys was measured using a Vickers micro hardness tester (HVS-1000, Yantai Huayin testing instrument Co., Ltd., China) with a load of 9.8 N for 10 s. The values of hardness were the average of

Testing surfaces of all samples were carefully mechanically abraded, polished, then ultrasonically cleaned in an alcohol solution and kept in a vacuum oven for 24 h. Anodic polarization test was performed in a standard three-electrode electrochemical cell, a saturated calomel electrode as the reference electrode (SCE), a platinum sheet as the auxiliary electrode (AE) and the samples as the working electrode (WE). Anodic polarization test was carried out in 0.5 mol/L H₂SO₄ solutions at room temperature using electrochemical test equipment (PGSTAT302 N, Switzerland) with a scanning speed of 2 mV/s. The tribocorrosion behaviors of the alloys were carried out using a ball-on-flat reciprocating sliding tribometer (MFT-4000, Lanzhou Institute of Chemical Physics, Chinese Academy of Sciences, Lanzhou, China) with a three-electrode system in 0.5 mol/L H₂SO₄ solutions at room temperature. NiTi/ AlNi₂Ti disk specimens were sliding against a 6 mm diameter balls made of Al₂O₃ ceramics (nominal hardness 20 GPa) for tribocorrosion testing. The 6 mm diameter Al₂O₃ balls were used as the counterparts due to its high hardness, high corrosion resistance and low electrical conductivity in H₂SO₄ solutions. High purity graphite is used as the counter electrode, the alloy samples are used as the working electrode, and a saturated calomel electrode is as the reference electrode, as shown in Fig. 1. In the tribocorrosion test, the load is loaded with weights, the sliding distance is adjusted by changing the eccentric distance between the connecting rod and the turntable, and the solution is added to the PTFE electrolytic cell by a dropper. A normal load 5 N was applied corresponding to the average hertzian contact pressure of 0.97 GPa at the alloys coupled with the Al₂O₃ ball. For the tribocorrosion tests under the condition of open circuit potential (OCP), the OCP was recorded for 5 min prior to a 20 min sliding wear test. The OCP continues to be recorded for 5 min after the end of the sliding test. The amplitude length and oscillation frequency are 5 mm and 1 Hz, respectively. Commercial traditional austenitic stainless steel OCr18Ni9 with a nominal chemical composition (wt %) of Fe-18.6%Cr-9.3%Ni-0.1%C was selected as a reference material for

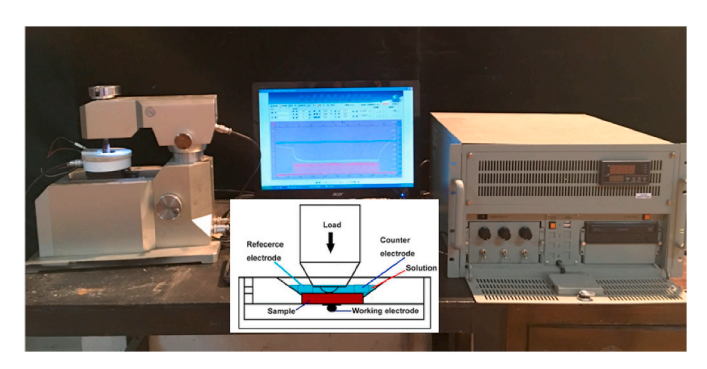


Fig. 1. The scheme diagram of tribocorrosion equipment.

tribocorrosion tests. The morphology of wear scars were investigated by Field-emission scanning electron microscopy (FESEM) and Transmission electron microscopy (TEM). TEM was undertaken in vacuum. The TEM images were acquired at an acceleration voltage of 200 kV. The chemical states of the elements of tribocorrosion surfaces were determined by Xray photoelectron spectroscopy (XPS) using a Kratos AXIS Ultra ESCA System with Al Ka (1486.6 eV) as the X-ray source. The accelerating voltage and emission current of the X-ray source were kept at 12 kV and 12 mA, respectively. The size of the analyzed sample area was 500 μm (spot diameter), and the total acquisition time is about 10 min. The base pressure of the sample analysis chamber was maintained at $\sim\!10^{-9}\,\text{mbar},$ the electron emission angle was 45° . The worn surfaces were sputtered by Ar⁺ for 8s before analysis (The Ar⁺ energy is 3000 eV, the etching area size is 2 mm (diameter), and the incident angle is 60°). Peak identification was performed by reference to an XPS database. The pass energy was selected to be 60 eV for survey scan and 20 eV for the features of interest (Al 2p, Ti 2p, Ni 2p, O 1s and C 1s) to ensure high resolution and good sensitivity.

3. Results

3.1. Microstructure

X-ray diffraction patterns of Al–Ni–Ti powder mixtures and arcmelted NiTi/AlNi $_2$ Ti alloys are shown in Fig. 2. It can be seen that the alloy samples are mainly composed of L2 $_1$ -AlNi $_2$ Ti alloy and ductile NiTi intermetallic. Those phases in Fig. 2 are based on the JCPDS file numbers 65–0380(Ni), 44–1294(Ti), 04–0787(Al), 65–4189(AlNi $_2$ Ti), 65–7711(B2–NiTi) and 65–0145(B19'-NiTi). There are two kinds of NiTi phases with cubic structure (B2–NiTi) and monoclinic structure (B19'-NiTi), indicating that part of the martensitic transformation of NiTi phase (B2 \rightarrow B19') is induced by arc machining and Al alloy components [281.

The typical microstructure of the alloy sample is shown in Fig. 3. It can be seen that the alloy has a uniform and compact microstructure and no obvious defects such as pores and microcracks. The average chemical composition (at. %) of the primary dendrites and interdendritic phases measured by SEM-EDS from at least three single measurements is shown in Fig. 4. Combined with the results of XRD analysis, it can be confirmed that the primary dendrite is AlNi₂Ti ternary intermetallic phase, the interdendritic phase is NiTi phase. In addition, XPS survey spectrum and high resolution XPS spectrum analysis of NiTi/AlNi₂Ti alloy surface were performed, as shown in Fig. 5. The surface of the alloy was

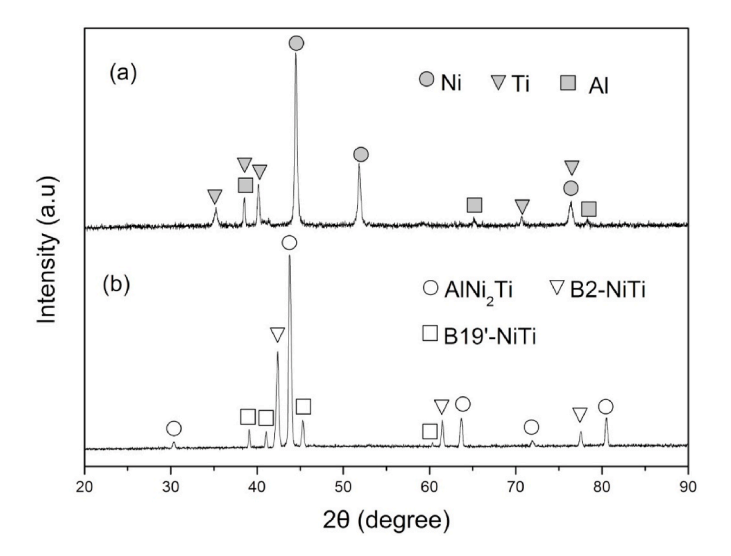
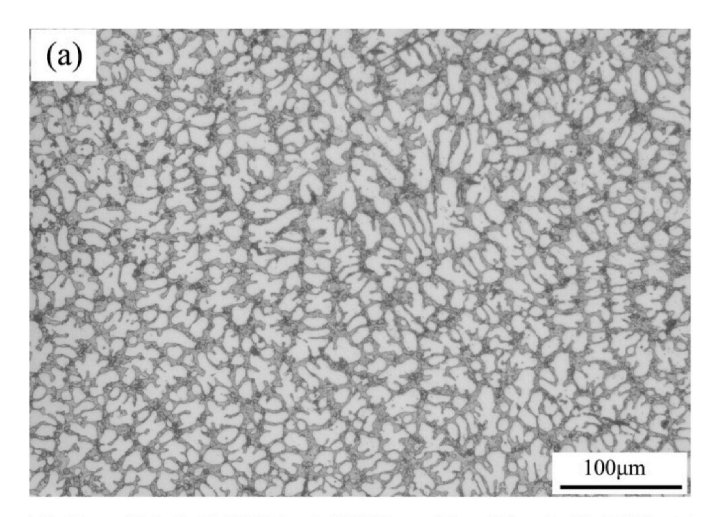


Fig. 2. X-ray diffraction pattern of the samples (a) Al–Ni–Ti powder mixture raw material and (b) $NiTi/AlNi_2Ti$ melted alloy.



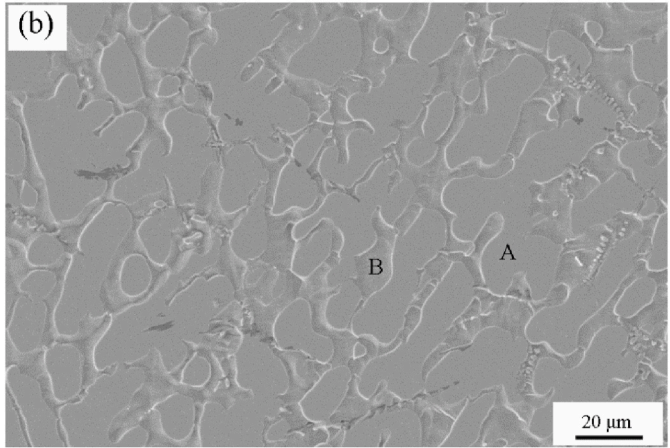


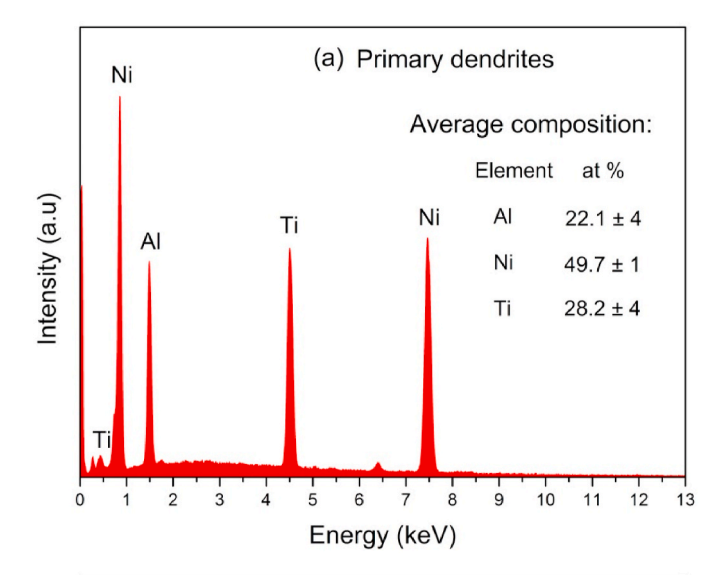
Fig. 3. Microstructure of $\rm NiTi/AlNi_2Ti$ intermetallic alloy (a) OM photograph and (b) SEM morphology.

sputtered with a 3 keV Ar⁺ ion beam for 600 s prior to XPS analyses to remove surface contamination. As shown in Fig. 5 (a), the XPS spectra exhibit peaks for Ni, Ti, Al and Ar. The Ar 2p and Ar 2s peaks possibly arise from the sputtering treatment of Ar⁺ ions on the alloy surface. In Fig. 5 (b, c and d), the binding energy of Al 2p (72.6 eV), Ni 2p (852.6 eV) and Ti 2p peaks (453.9 eV, 460.0 eV) were assigned to the metallic state (Al, Ni and Ti) without oxidized distribution [1]. It is worth noting that no oxygen element or oxides of Al, Ni and Ti were detected in Figs. 2, Figs. 4 and 5, indicating that the NiTi/AlNi₂Ti alloy was not contaminated by oxygen in the environment. This is mainly due to the high vacuum level and a small amount of high-purity argon protection during powder mixing and alloy melting. The volume fraction of the primary dendrite of AlNi₂Ti is determined to be about 58% according to the SEM morphology of Fig. 3.

In the Al–Ni–Ti ternary alloy system, the $AlNi_2Ti$ intermetallic compound has a higher melting point, and firstly precipitates from the liquid phase to form a primary dendritic phase during arc melted and subsequent rapid solidification of the circulating water-cooled copper crucible. With the precipitation of $AlNi_2Ti$ phase, Ni and Ti elements are gradually enriched in residual liquids and transformed into NiTi phase. The average hardness of the $NiTi/AlNi_2Ti$ alloy was tested to be approximately 810 HV due to the high volume fraction of the high hardness $AlNi_2Ti$ intermetallic compound.

3.2. Tribocorrosion behavior of the NiTi/AlNi₂Ti alloy

Anodic potentiodynamic polarization curves of the NiTi/AlNi₂Ti alloy and the reference materials 0Cr18Ni9 in 0.5 mol/L $\rm H_2SO_4$ solution



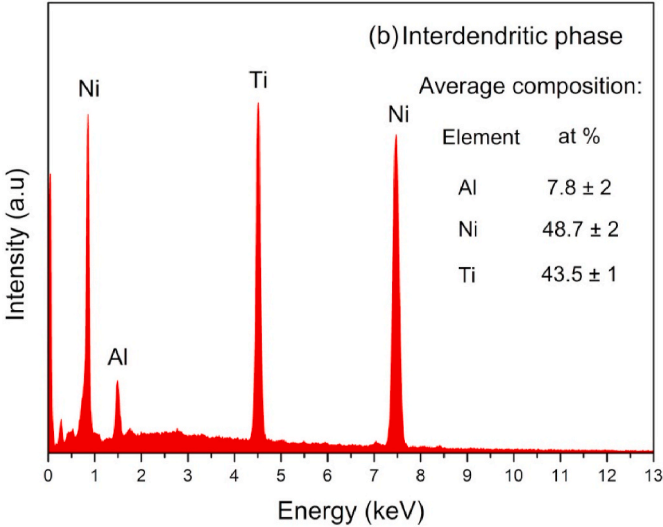


Fig. 4. EDS analysis results of primary dendrites (a) and interdendritic phase (b) of intermetallic NiTi/AlNi $_2$ Ti alloy in Fig. 3. The average composition (at. %) is obtained from at least three different locations of the alloy.

are shown in Fig. 6. It can be seen that the polarization curves of the two materials show a similar in shape. The anode current density of the two materials gradually increased in the activated dissolution region from open circuit potential to a passive potential. Subsequently, the current density decreases obviously due to the passivation of the material surface in 0.5 mol/L $\rm H_2SO_4$ solution. The current density of the two materials increases gradually after a wide passive range on the anodic polarization curve, suggesting the breakdown of the passive film. However, compared to the reference material OCr18Ni9, the NiTi/AlNi_2Ti alloy has a higher corrosion potential, a much wider passivation range (from 0.1 V to 1.2 V) and a lower passive current density (about $10^{-5} \rm A/cm^2)$, and its breakdown potential is 400 mV higher than OCr18Ni9 stainless steel, showing that the NiTi/AlNi_2Ti alloy has excellent corrosion resistance in a 0.5 mol/L $\rm H_2SO_4$ solution.

In order to elucidate the synergistic effect of corrosion and wear, the tribocorrosion behavior of NiTi/AlNi $_2$ Ti alloy and reference material 0Cr18Ni9 was studied by sliding against Al $_2$ O $_3$ ceramic ball in 0.5 mol/L H $_2$ SO $_4$ solution. Fig. 7 shows the variation of friction coefficients of NiTi/AlNi $_2$ Ti alloy and 0Cr18Ni9 during sliding test in deionized water and H $_2$ SO $_4$ solution. During the whole sliding process, the NiTi/AlNi $_2$ Ti alloy exhibited a relatively stable wear performance with a constant friction coefficient of 0.16 and 0.17 in deionized water and H $_2$ SO $_4$

solution, respectively. However, austenitic stainless steel 0Cr18Ni9 shows an unstable wear performance with a coefficient significant fluctuation and a higher friction coefficient. It is worth noting that all samples show a higher sliding friction coefficient in H_2SO_4 solution than in deionized water. In the synergy of wear and corrosion, it is difficult to form three-body rolling and oxide lubrication due to erosion or flushing of wear debris, which leads to the increase of friction coefficient in H_2SO_4 solution.

Fig. 8 is a typical tribocorrosion curve with corresponding open circuit potentials (OCP) of the NiTi/AlNi $_2$ Ti alloy in $\rm H_2SO_4$ solution. It can be seen that NiTi/AlNi $_2$ Ti alloy exhibits a stable friction coefficient of 0.16 during the whole tribocorrosion period, indicating that the alloy has an excellent tribocorrosion resistance in 0.5 mol/L $\rm H_2SO_4$ solution. At the same time, the alloy maintained a relatively stable OCP of 0.003 V during soaking and only decreased by 0.01 V at the initial stage of tribocorrosion and then gradually increased by 0.01 V at the end of the tribocorrosion period. Subsequently, the OCP of the alloy increased rapidly to 0.063 V during passivation, which indicated that the alloy had strong passivation ability in $\rm H_2SO_4$ solution.

Fig. 9 shows the continuous evolutions of OCP and current density of NiTi/AlNi₂Ti alloy and reference material 0Cr18Ni9 in H₂SO₄ solution during immersion, tribocorrosion and passivation. It is evident that the OCP and current density curves of all samples are similar in shape, indicating that they follow a similar tribocorrosion mechanism. As can be seen from Fig. 9 (a), the initial potential of the reference material 0Cr18Ni9 is more negative and gradually declines with the increase of soaking time. In contrast, the initial potential of NiTi/AlNi2Ti alloy is more positive than that of 0Cr18Ni9 and gradually stabilizes with the increase of immersion time. This is mainly attributed to the formation of dense passivation films (such as Al₂O₃ and TiO₂) on the surface of the alloy. The potential values of NiTi/AlNi2Ti alloy and 0Cr18Ni9 are decreased significantly as soon as the Al₂O₃ ball came into contact with the surface of the sample. At the same time, the tribocorrosion results in a more negative potential of 0Cr18Ni9 with a significant fluctuations than that of NiTi/AlNi₂Ti alloy. When the sliding stops, the OCP of NiTi/ AlNi₂Ti alloy and 0Cr18Ni9 increases gradually, indicating that the passivation film on the surface of the sample has been reconstructed. The evolution of the current density of the samples was studied during tribocorrosion, as shown in Fig. 10 (b). For NiTi/AlNi₂Ti alloy, the corrosion current density is negative during soaking, indicating no corrosion occurred. Once the sliding starts, the current increases significantly, which is mainly attributed to the wear-accelerating corrosion. After the sliding stops, a gradual decrease in the current of the alloy and 0Cr18Ni9 was observed. This may be related to the decrease of the activation area caused by the re-passivation of the sample surface.

Unlike the continuous sliding process, in the reciprocating sliding, the surface shearing occurs and the friction changes in the opposite direction alternately, which also leads to the corresponding change of OCP at different contact positions. In order to better clarify the tribocorrosion characteristics of the NiTi/AlNi₂Ti alloy at different contact positions of the sliding stroke, Fig. 10 shows the tribocorrosion curves of the NiTi/ AlNi2Ti alloy at a lower vibration frequency of 0.2 Hz in 0.5 mol/L H₂SO₄ solution. It is interesting to note the definite pattern of friction coefficient variation for each cycle in Fig. 10 (b). The friction coefficient increases at both edge of the sliding stroke due to the instantaneous impact of the ends and the increase of static adhesion. However, relatively mild friction conditions were observed at the center of the stroke. Because a unidirectional friction coefficient sensor is used in this experiment, the adjacent reverse stroke friction coefficient is not shown. At the same time, this also causes the output signal of the OCP to change according to the position of the sliding contact. The decrease in OCP value is proportional to the increase in friction coefficient (friction force), as shown in Fig. 10 (b). The OCP decreases during the sliding contact (the central area of the stroke), the OCP value increases significantly as the friction coefficient reduces to zero (at the edge of the

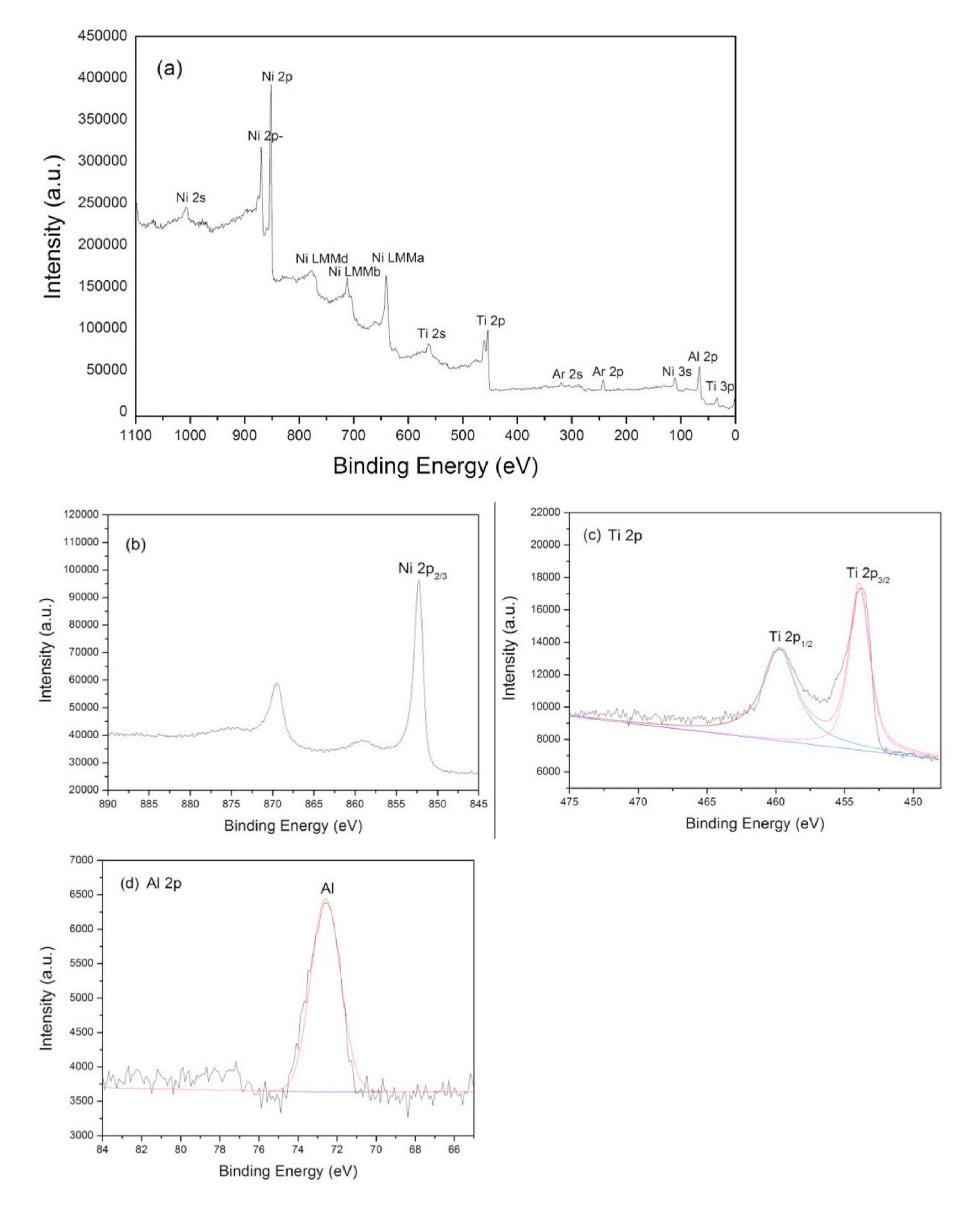


Fig. 5. XPS survey spectra (a) and high-resolution XPS spectra (b, c and d) of NiTi/AlNi₂Ti alloy surface sputtered with Ar⁺ ion for 600 s.

sliding stroke). This phenomenon can be attributed to the synergistic interaction of force and corrosion. This is consistent with the results of Chen and Xie et al. [6,29].

Fig. 11 shows a typical three-dimensional optical morphology and cross-sectional profile of the wear tracks of NiTi/AlNi2Ti alloy and OCr18Ni9 after tribocorrosion test in H₂SO₄ solution. As shown in Fig. 11 (a), NiTi/AlNi₂Ti alloy shows a very smooth wear track in H₂SO₄ solution with a cross-section area of 0.00032 mm². In contrast, the reference material 0Cr18Ni9 suffered from severe tribocorrosion damage in the H₂SO₄ solution accompanied by a wider and deeper wear track with a cross-section area of 0.0036 mm², as shown in Fig. 11 (b). The wear volumes of NiTi/AlNi2Ti alloy and 0Cr18Ni9 alloy in H2SO4 solution and deionized water were calculated by measuring the crosssectional area and length of wear marks, as shown in Fig. 12. It can be seen that the wear volumes of the two experimental materials under the tribocorrosion test are higher than that of sliding wear in deionized water. In particular, the wear volume of the reference material OCr18Ni9 under tribocorrosion condition is three times higher than that of sliding wear in deionized water, indicating the synergistic effect of corrosion on wear-loss. In addition, the wear volume of NiTi/AlNi $_2$ Ti alloy is much lower than that of reference material 0Cr18Ni9 (about 10

times lower) due to higher hardness and higher corrosion resistance under tribocorrosion conditions. That is to say, NiTi/AlNi₂Ti alloy is more suitable as tribocorrosion resistance material in $0.5 \text{ mol/L H}_2SO_4$ solution than reference material OCr18Ni9.

Fig. 13 shows the wear scar morphologies of the samples after the tribocorrosion test. As shown in Fig. 13 (a), the reference material 0Cr18Ni9 exhibits a poor tribocorrosion resistance in H₂SO₄ solution. The wear surface of 0Cr18Ni9 is rough with a large amount of black wear and corrosion products in the wear track, as shown in Fig. 13 (c). The corrosion resistance of the material system is highly related to surface defects. Obvious wear defects such as ploughs, debris and cracks can be observed on the worn surface of 0Cr18Ni9, indicating that the wear mechanism is abrasive wear and plastic deformation. This also explains that 0Cr18Ni9 has a low corrosion potential and high corrosion current. At the same time, in an enlarged micro-morphology (Fig. 13 (e)), there are a large number of small pits in the sliding direction, which roughens the tribo-pair interface, resulting in higher contact stress and larger wear loss. On the other hand, the rough interface caused by etching pits can also cause a micro-galvanic cell to accelerate the corrosion process. In addition, these pits may be the nucleation site of cracks, promoting the initiation and propagation of cracks, and

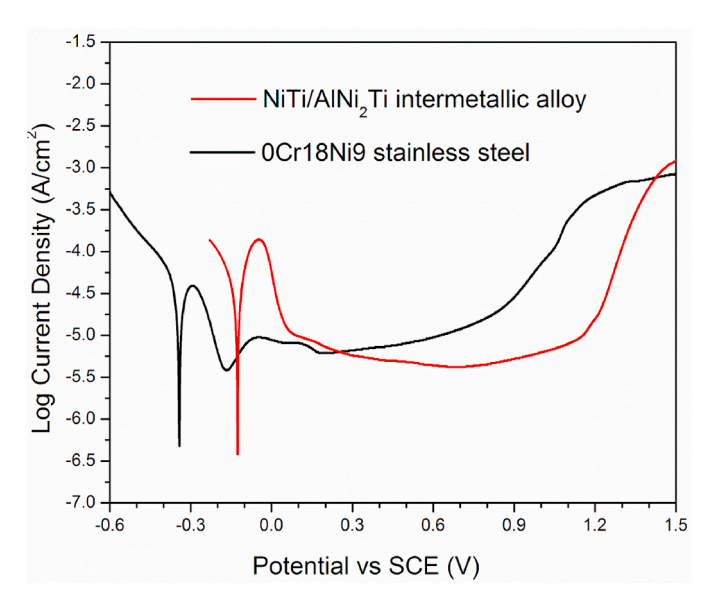


Fig. 6. Anodic potentiodynamic polarization curves of the $NiTi/AlNi_2Ti$ alloy and the stainless steel 0Cr18Ni9 in 0.5 mol/L H_2SO_4 solution.

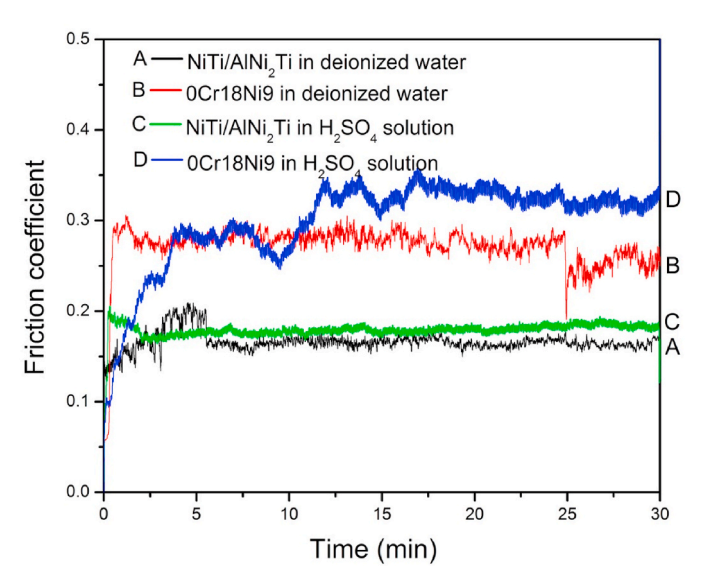


Fig. 7. Friction coefficient of $NiTi/AlNi_2Ti$ alloy and reference material 0Cr18Ni9.

intensifying the synergistic effect between wear and corrosion. In contrast, the wear surface of NiTi/AlNi₂Ti alloy is relatively smooth, and no tribocorrosion defects such as furrows, spalling and large pits are observed, indicating that the alloy has excellent tribocorrosion resistance in 0.5 mol/L H₂SO₄ solution. Unlike the outer part of the wear scar, a typical microstructures consisting of the primary phase and interdendritic phase are found at the wear track, similar to metallographic corrosion, as shown in Fig. 13 (d). This difference can be attributed to wear-accelerated corrosion. More in-depth observation shows that the plastic NiTi intergranular phase with the apparent deformed microparticle distributing dispersive in the wear track (Fig. 13 (e)), indicating the wear mechanism is dominated by micro-plastic deformation. In addition, some tiny pits appear at the interface of the two phases in Fig. 13(e), which can be attributed to the wear contact stresses accelerating corrosion effect, resulting in the microparticle pulling out of the wear surface. The EDS analysis results of Fig. 13 (g) and (h) showed that Al, Ni, Ti and O elements and a small amount of black (Al-O) tribocorrosion products exist on the wear surface of the

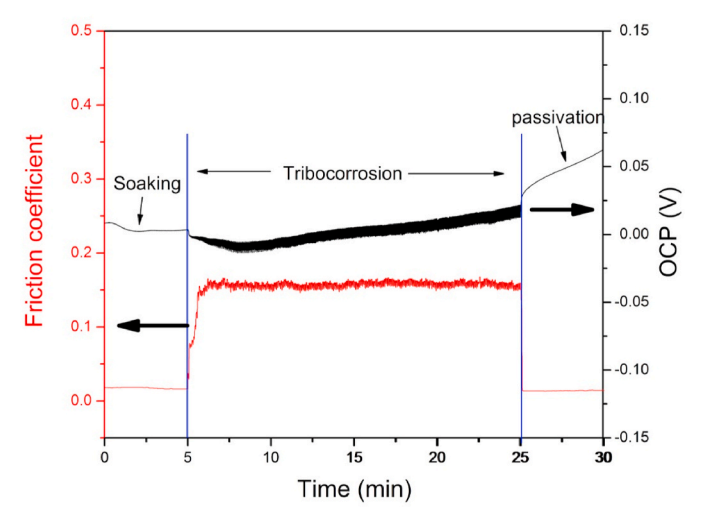


Fig. 8. Tribocorrosion curve with the corresponding OCP of the $NiTi/AlNi_2Ti$ alloy in 0.5 mol/L H_2SO_4 solution.

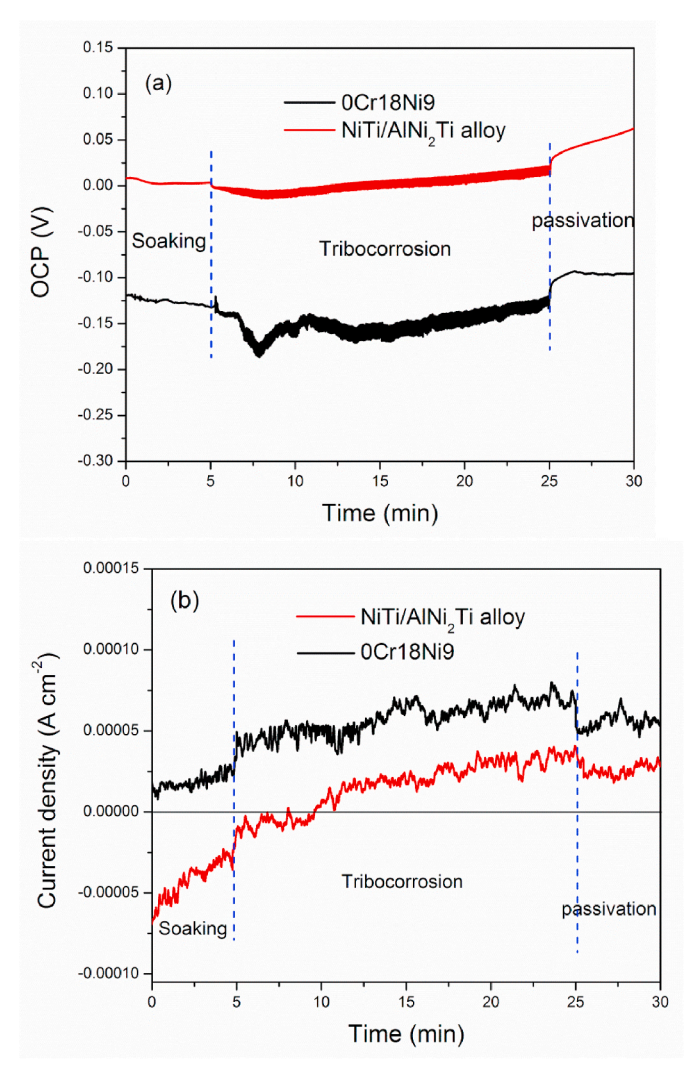


Fig. 9. Evolution of OCP (a) and current density (b) of NiTi/AlNi₂Ti alloy and 0Cr18Ni9 during tribocorrosion tests in $0.5\ mol/L\ H_2SO_4$ solution.

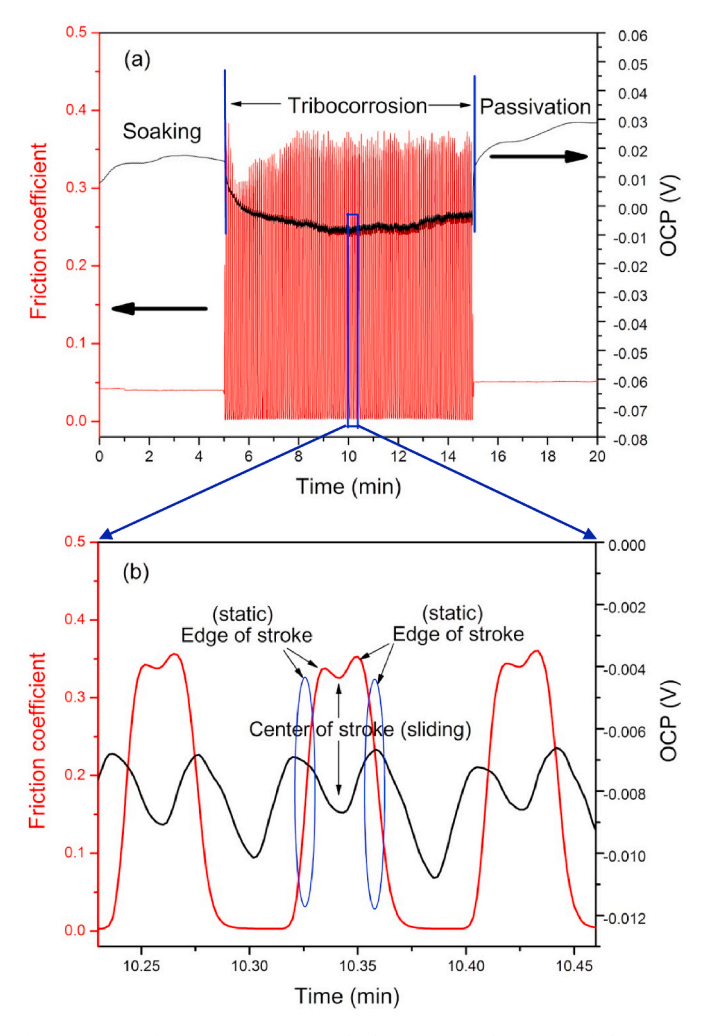


Fig. 10. (a) Tribocorrosion curve with the corresponding OCP of the NiTi/AlNi_2Ti alloy with an oscillation frequency of 0.2 Hz in 0.5 mol/L $\rm H_2SO_4$ solution; (b) Partial magnification of the tribocorrosion curve in Fig. 9 (a).

 $NiTi/AlNi_2Ti$ alloy. The wear surface of the coatings was demonstrated to contain oxygen in Fig. 13(g) and (h), which indicated that a tribochemical reaction occurred.

In order to further determine the surface composition of the alloy, XPS analysis was carried out on the surface of NiTi/AlNi₂Ti alloy before and after tribocorrosion test in 0.5 mol/L H₂SO₄ solution. As shown in Fig. 14, the wide scan spectra exhibit peaks of aluminum, nickel, titanium, oxygen and carbon. The C 1s peak possibly arose from a contaminant hydrocarbon layer covering the specimen surface [30]. According to the G. Greczynski and L. Hultman [31], the binding energy scale referencing based on the C 1s peak of adventitious carbon is highly arbitrary due to the unknown origin and composition of the adventitious carbon. The binding energy value of adventitious carbon (C-C, C-H, C-O, C-F) varies in the range 284.0-285.6eV. Therefore, the Ni 2p peak at 852.6 eV, corresponding to Ni in metallic state, was used as a reference [30]. Fig. 15 shows high-resolution XPS spectra for the Al 2p, Ni 2p, Ti 2p, O 1s and C 1s peaks collected from the original NiTi/AlNi₂Ti alloy and after tribocorrosion test in 0.5 mol/L H₂SO₄ solution. In Fig. 15(a) and (c), the Al 2p and Ti 2p_{3/2} spectra for the original NiTi/AlNi₂Ti alloy consisted of two peaks, respectively. The peak at low binding energy of 72.6 eV and 453.9 eV were assigned to the metallic state (Al and Ti), and the peak at high binding energy of 74.3 eV and 458.68 eV were assigned to the oxidation state (Al₂O₃ and TiO₂). Part of the existence of Al₂O₃ and TiO_2 can be attributed to the spontaneous surface oxidation of Tiand Al when exposed to the atmosphere. After tribocorrosion test, a

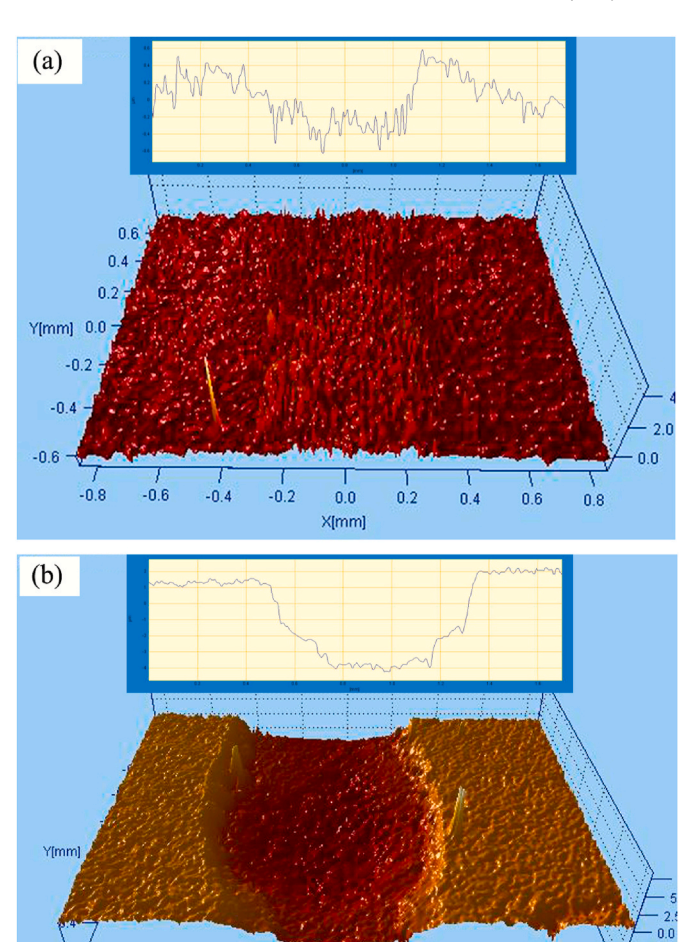


Fig. 11. The three-dimensional optical morphology and cross-sectional profile of tribocorrosion scar of NiTi/AlNi $_2$ Ti alloy(a) and reference material 0Cr18Ni9 (b) in 0.5 mol/L $_2$ SO $_4$ solution.

0.0

0.6

-0.4

-0.6

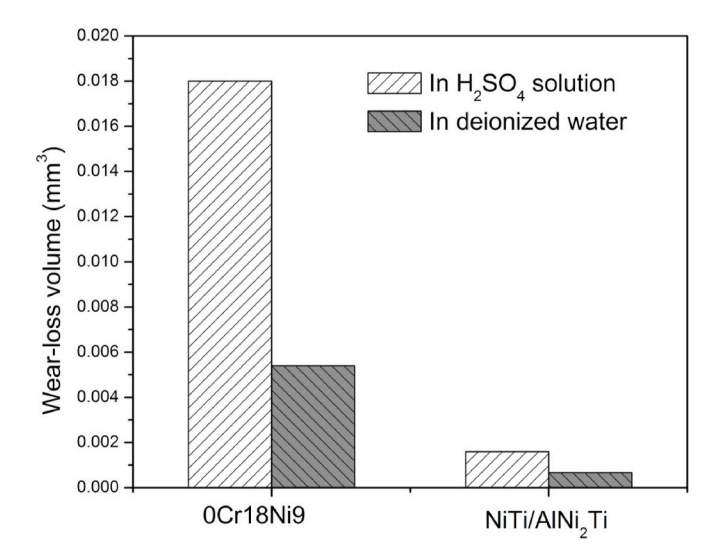


Fig. 12. Wear volumes of the NiTi/AlNi $_2$ Ti alloy and reference material 0Cr18Ni9 in 0.5 mol/L $\rm H_2SO_4$ solution and deionized water.

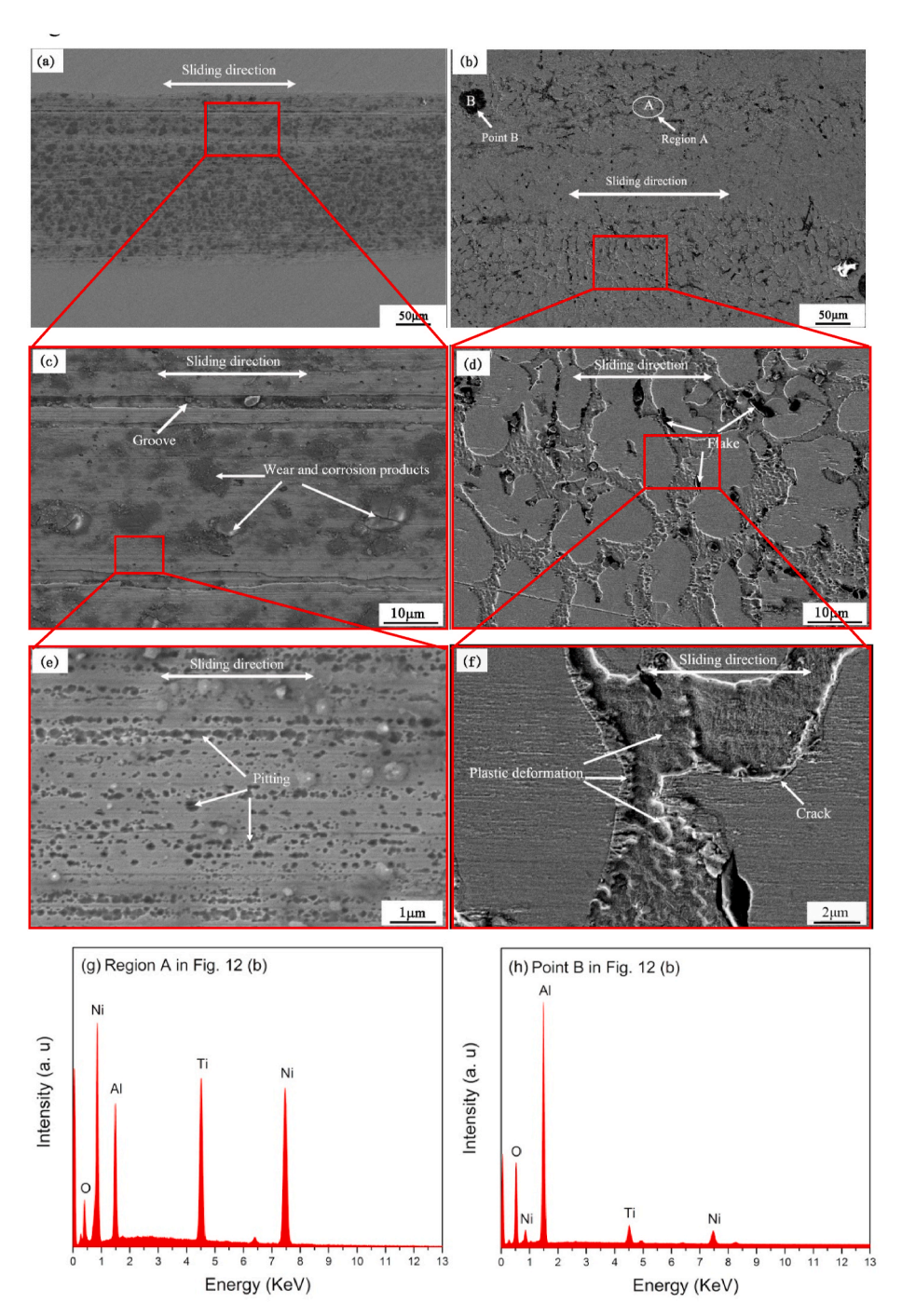


Fig. 13. SEM images of the wear track of the reference material 0Cr18Ni9 (a, c and e) and $NiTi/AlNi_2Ti$ alloy (b, d and f) after the tribocorrosion test in 0.5 mol/L H_2SO_4 solution; (g, h) EDS analysis of region A and point B in Fig. 12 (b).

single Al 2p peak is located at the binding energy of 74.3 eV (Fig. 15(a)), indicating that Al is in the form of Al_2O_3 on the surface of the sample [32]. The Ni 2p spectra (Fig. 15(b)) shows a photoemission signal at 852.6 eV and no signal corresponding to Ni^{2+} ions, indicating that the chemical state of Ni corresponds to the elemental Ni without oxidized distribution [30]. In Fig. 15(c), the spectrum of Ti 2p is composed of Ti 2p_{3/2} and Ti 2p_{1/2} doublet peaks at 458.68 eV and 463.98 eV, which corresponds to the TiO₂ phase [33]. Moreover, the O 1s peak in Figs. 14 (b) and Fig. 15(d) had a stronger intensity after tribocorrosion test than that of the original NiTi/AlNi₂Ti alloy, suggesting that the tribocorrosion test in 0.5 mol/L H_2SO_4 solution led to the formation of Al_2O_3 and TiO₂ in the surface passive film.

In order to better understand the wear mechanism, the wear debris of

NiTi/AlNi₂Ti alloy after tribocorrosion test in $0.5 \, \mathrm{mol/L} \, H_2 \mathrm{SO_4}$ solution and sliding in deionized water were studied using the HRTEM technique. TEM micrograph (Fig. 16(a)) and its corresponding diffraction pattern (Fig. 16(b)) demonstrated that the B2–NiTi phase transformed into a martensitic B19'- NiTi phase during the tribocorrosion process. The HRTEM micrograph in Fig. 16(c) revealed that some lattices of the NiTi particles were severely distorted, which indicates that the local plastic deformation was induced during the tribocorrosion test. For the wear debris of the alloy obtained from sliding in deionized water, its TEM and HRTEM images and corresponding FFT patterns were shown in Fig. 16 (d) and (e). The measured lattice spacings of the wear debris were 0.2132 nm, 0.292 nm and 0.2302 nm, which were in good agreement with the (110) plane of B2–NiTi (PDF No. 65–7711), (100) plane of

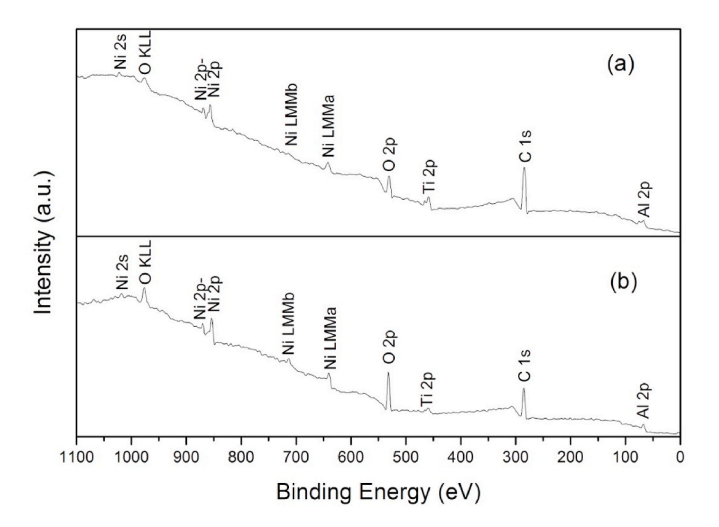


Fig. 14. XPS survey spectra of the original NiTi/AlNi $_2$ Ti alloy (a) and after tribocorrosion test in 0.5 mol/L $\rm H_2SO_4$ solution (b).

 $AlNi_2Ti$ (PDF No. 65–4198) and (101) plane of B19'- NiTi (PDF No. 65–7711), respectively. At the same time, obvious lattice distortion is also found in the interior of B2–NiTi particles due to the plastic deformation caused by reciprocating friction.

4. Discussion

The results of the tribocorrosion test show that the NiTi/AlNi₂Ti alloy has better tribocorrosion resistance compared to the reference material 0Cr18Ni9 during the whole tribocorrosion tests. In Fig. 7, the NiTi/AlNi₂Ti alloy shows a significantly lower and stable friction coefficient than that of the 0Cr18Ni9 material during the tribocorrosion test in 0.5 mol/L $\rm H_2SO_4$ solution. According to Murthy's research [34], the friction coefficient during sliding is mainly related to the surface state of the friction contact area. As Fig. 13 indicates, the wear surface of the NiTi/AlNi₂Ti alloy is relatively smooth, while the wear surface of 0Cr18Ni9 has a large amount of black tribocorrosion products, furrows and a large number of small pits in the wear track, which roughens the tribo-pair interface and leads to the increase and fluctuation of friction coefficient.

In Fig. 9, the NiTi/AlNi₂Ti alloy and 0Cr18Ni9 material exhibited a significant decrease in open circuit potential and increase in corrosion current density during sliding tribocorrosion, which was attributed to

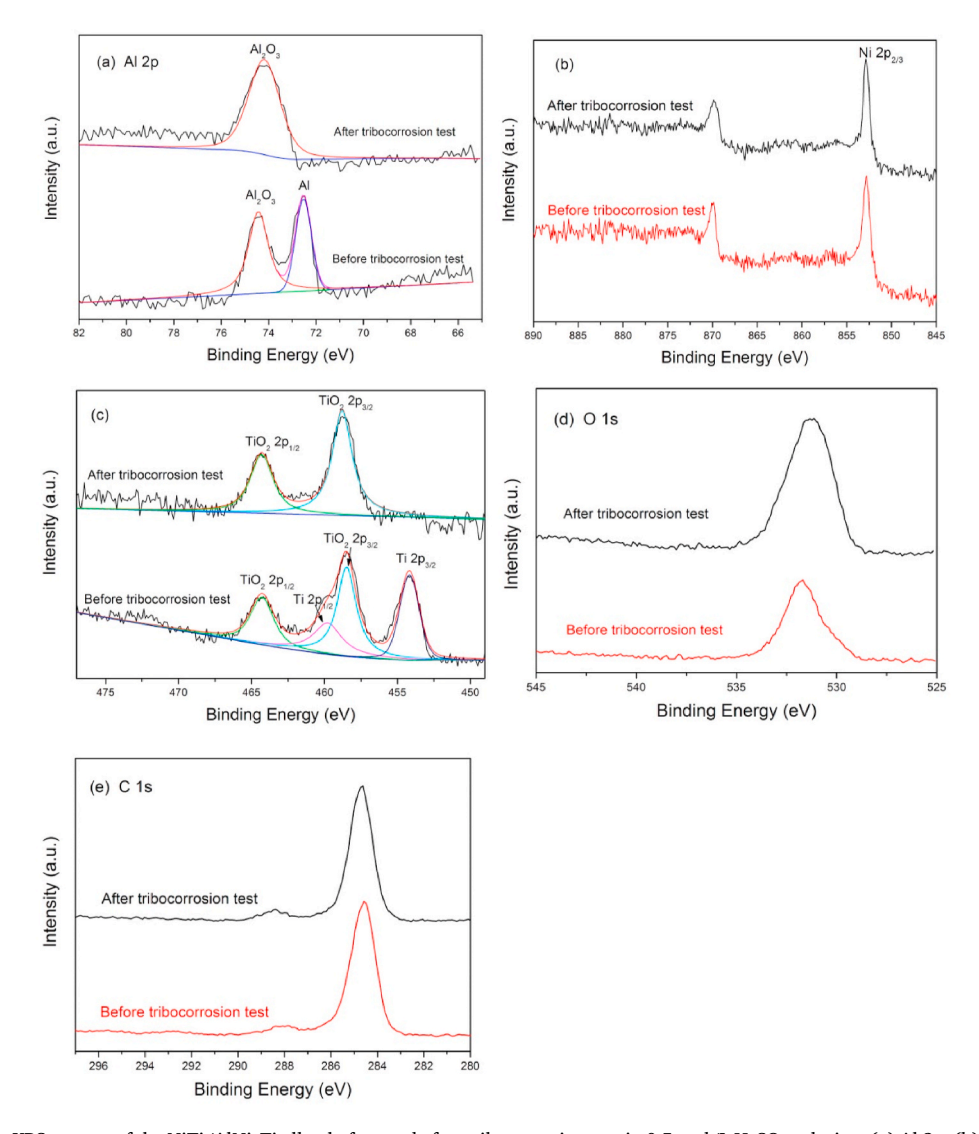


Fig. 15. High-resolution XPS spectra of the NiTi/AlNi₂Ti alloy before and after tribocorrosion test in $0.5 \text{ mol/L H}_2SO_4$ solution: (a) Al 2p, (b) Ni 2p, (c) Ti 2p, (d) O 1s and (e) C 1s.

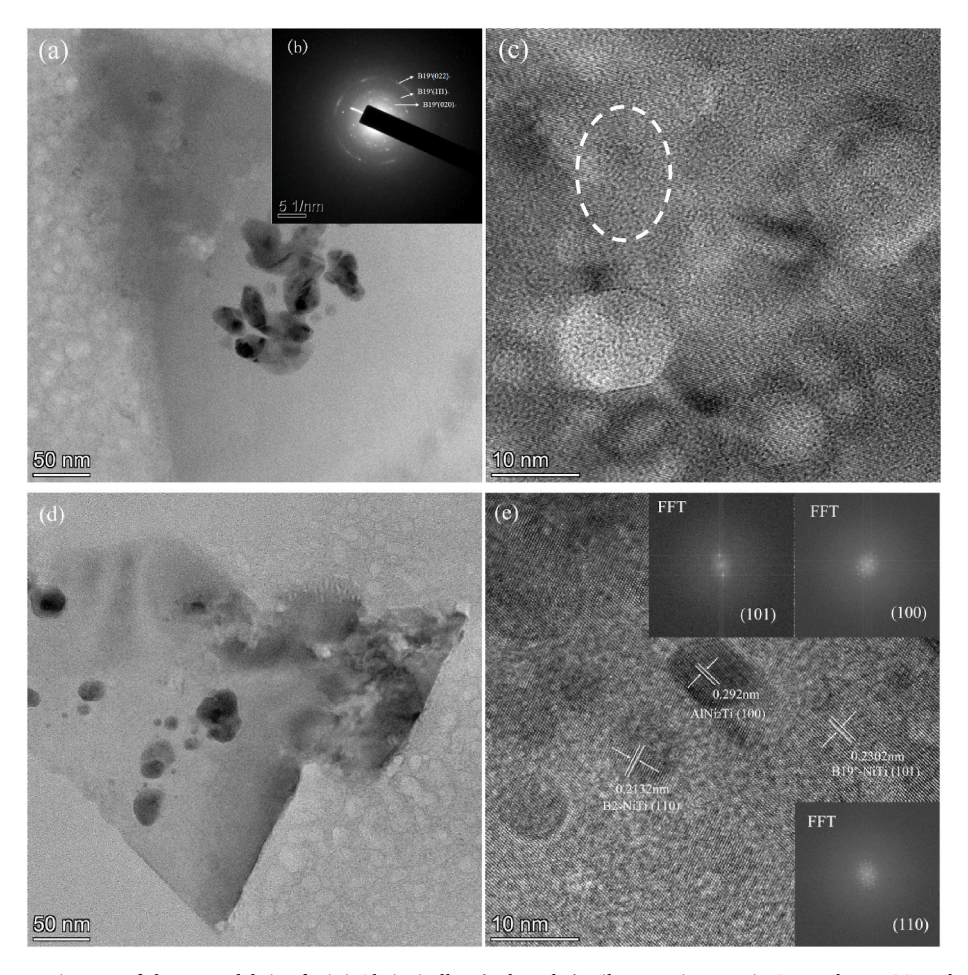


Fig. 16. (a) TEM and HRTEM images of the wear debris of NiTi/AlNi₂Ti alloy (a, b and c) tribocorrosion test in 0.5 mol/L H_2SO_4 solution and (d, e) sliding in deionized water. (Insets: FFT patterns of the corresponding regions.)

obvious wear accelerated corrosion. Generally, the decrease in corrosion potential and increase in corrosion current indicate an increase in corrosion tendency of the materials surface. According to the research of Ponthiaux et al. [35], there are four key parameters affecting the evolution of potential and current during the sliding: (a) the intrinsic corrosion potentials of the worn and unworn surfaces; (b) the ratio between the worn and unworn surface areas; (c) the relative position of worn and unworn areas; (d) the mechanisms and kinetics of the involved reactions. According to the XPS results in Fig. 15, a dense passivation film (Al₂O₃ and TiO₂) has been formed on the surface of the NiTi/Al-Ni₂Ti alloy during tribocorrosion. Once the sliding starts, the passive film is continuously broken leading to surface depassivation and the fresh alloy surface has high electrochemical activity. This leads to significant metal dissolution and reduction in corrosion potential. Moreover, removal of the passive film and the increase in surface area that was exposed to the solution during the sliding motion also increased the corrosion current of the material [36]. This is consistent with the study by Ma et al. [37], for passivation materials, the current tends to increase due to wear damage of the passivation film during the sliding process. On the other hand, the mechanically destroyed passivated surface (anode) and the surrounding passivated surface (cathode) can form a galvanic cell [37,38], which further reduces the corrosion resistance of the material. In addition, the OCP of the NiTi/AlNi2Ti alloy is more positive and stable than 0Cr18Ni9 during tribocorrosion as shown in Fig. 9 (a). The hardness and chemical stability of materials are also important factors affecting corrosion and wear. NiTi/AlNi₂Ti alloy has a higher hardness than 0Cr18Ni9, which results in a lower cathode area owing to the formation of a narrower wear track on the surface of the alloy during sliding. Furthermore, the NiTi/AlNi2Ti alloy has superior

chemical stability and strong internal atomic bonding, so the galvanic corrosion of the alloy is slighter than that of 0Cr18Ni9.

It can be seen from Fig. 12 that the wear volume of NiTi/AlNi₂Ti alloy and 0Cr18Ni9 material under the tribocorrosion test is higher than that of sliding wear in deionized water, indicating the synergistic effect of corrosion on wear-loss. During the tribocorrosion test, the oxide film formed is not thick enough at each contact interval of 0.5 s. The corrosion accelerated wear (Vcw) comes from the repeated removal of the thin oxide film by subsequent sliding cycles results in larger chemical wear. On the other hand, due to the low hardness of the 0Cr18Ni9 stainless steel and the high sliding contact pressure, the Al₂O₃ ball digs through the oxide film into the substrate easily to form the larger and rougher wear track area, which results in a larger wear volume of 0Cr18Ni9 than that of NiTi/AlNi2Ti alloy under tribocorrosion conditions. In Fig. 13, the plastic NiTi intergranular phase undergoes obvious plastic deformation, and the wear mechanism is dominated by the micro-plastic deformation of the NiTi phase. As shown in Fig. 2, the NiTi phase in the melted NiTi/AlNi₂Ti alloy is mainly B2-NiTi phase with austenitic structure. The HRTEM images obtained from the wear debris of NiTi/AlNi₂Ti alloy as presented in Fig. 16 demonstrated that the B2-NiTi phase transformed into a martensitic B19'- NiTi phase during the wear process. However, heavy plastic deformation occurred in the worn surface as a result of the wear test stabilized the martensitic B19'-NiTi phase to the B2-NiTi phase after wear test and restricted the pseudoelasticity property [26].

In order to understand the synergistic tribocorrosion mechanism, the material loss ($\triangle V$) due to the synergistic effect between wear and corrosion was calculated according to the following formula [39]:

Where V_t is the total material loss during tribocorrosion testing, V_w is material loss due to pure mechanical wear (sliding in deionized water), V_c is material loss due to static corrosion without wear. For passivated materials, V_c is usually negligible compared to the magnitude of total wear loss [40]. The V_t and V_w obtained in Fig. 12 are introduced into formula (2), and the ΔV of the NiTi/AlNi₂Ti alloy and the 0Cr18Ni9 material are calculated to be 9.3E-4 and 1.25E-2, respectively. The smaller ΔV of the NiTi/AlNi₂Ti alloy shows a better tribocorrosion resistance compared to 0Cr18Ni9 material. The synergistic effect ratio (ΔV/V_t) of NiTi/AlNi₂Ti alloy and 0Cr18Ni9 material is 58.1% and 69.4%, respectively. The material loss is dominated by the synergistic effect of corrosion and wear. In addition, the material loss ΔV can be further divided into two components: corrosion accelerated wear (V_{cw}) and wear accelerated corrosion (Vwc). In tribocorrosion test, the material loss of wear accelerated corrosion (Vwc) can be given by Faraday's law [41]:

$$V_{wc} = \frac{ItM}{nF\rho}$$
 (3)

where I is the current during the tribocorrosion test, the current value can be estimated from Fig. 9 (b) under sliding. t is test time, F is the Faraday's constant (96,500C/mol) and ρ is the density of the material. M is the atomic mass of the alloy given by $\sum X_i M_i$, where X_i is the mole fraction and M_i is the atomic mass of the alloy constituents (Al, Ti and Ni). n is the number of electrons transferred from the dissolution of one atom of the corroded material, it depends on the specific anodic reactions involved. For 0Cr18Ni9 stainless steel, n = 2 was used for calculations [42]. For NiTi/AlNi2Ti alloy in the active region, both Al and Ti dissolve with a low valence of 2, and in the passive region they form oxides with a valence of 3 and 4, respectively. If n = 2 is used, an upper bound will be obtained for V_{wc} ; while if n=4, a lower bound will be obtained for Vwc. It is difficult to determine the exact valence value under the test condition [43]. Based on the observation that "instantaneous passivation and re-passivation" is maintained during the tribocorrosion test (in Fig. 8), a valence value (n) of 3 is used to account for oxide film formation and passive dissolution at contact intervals. V_{cw} cannot be obtained directly, but it can be estimated according to V_{cw} = $\Delta V - V_{wc}$. The V_{wc} and V_{cw} of NiTi/AlNi₂Ti alloy and 0Cr18Ni9 material are (1.08E-4 mm³, 8.22E-4 mm³) and (2.58E-3 mm³, 9.92E-3 mm³), respectively. The V_{cw} of the two materials is much larger than that of Vwc, indicating that corrosion accelerated wear (Vcw) is the main synergistic mechanism.

5. Conclusions

Microstructure and tribocorrosion properties of NiTi/AlNi $_2$ Ti intermetallic alloy were investigated by tribocorrosion test in 0.5 mol/L H_2SO_4 solution. The following conclusions can be drawn:

- A novel corrosion-resistant NiTi/AlNi₂Ti intermetallic alloy was fabricated by arc melting process with a microstructure consisting of the primary dendrites AlNi₂Ti and interdendritic phase of NiTi.
- (2) The tribocorrosion test results showed that the OCP of NiTi/AlNi₂Ti alloy decreases as the sliding starts and then gradually increases during the passivation, and the decrease in the OCP value is proportional to the increase in the frictional force, indicating a strong wear-corrosion synergistic effect. The current density of NiTi/AlNi₂Ti alloy increases as the sliding starts due to the destruction of a passive film and the increase of contact area (wear accelerated corrosion). The wear volume of NiTi/AlNi₂Ti alloy and 0Cr18Ni9 material under the tribocorrosion test is higher than that of sliding in deionized water due to the synergistic acceleration process of wear and corrosion.

(3) The excellent electrochemical corrosion resistance of the alloy is mainly due to the instantaneous formation of a stable and compact passive film composed of TiO₂ and Al₂O₃. The NiTi/AlNi₂Ti alloy has better tribocorrosion resistance than the 0Cr18Ni9 material in the 0.5 mol/L H₂SO₄ solution with a high OCP, low corrosion current and low wear volume. The wear volume of NiTi/AlNi₂Ti alloy is about 10 times lower than that of reference material 0Cr18Ni9. The wear mechanism of the test materials is abrasive wear and plastic deformation. The V_{cw} of the two materials is much larger than that of V_{wc}, indicating that corrosion accelerated wear (V_{cw}) is the main synergistic mechanism.

Declaration of competing interest

The authors declare that they have no known competing financial interests or personal relationships that could have appeared to influence the work reported in this paper.

Acknowledgments

This research was supported by the Natural Science Foundation of Shandong Province of China (Grant Nos. ZR2018MEM005), National Natural Science Foundation of China (Grant No. 51701091). The authors acknowledge Mr Deshun Liu for their assistance on experiments of annealing.

References

- [1] L. Yuan, H.M. Wang, Corrosion behaviors of a γ-toughened Cr₁₃Ni₅Si₂/Cr₃Ni₅Si₂ multi-phase ternary metal silicide alloy in NaCl solution, Electrochim. Acta 54 (2008) 421–429.
- [2] L.X. Dong, H.M. Wang, Microstructure and corrosion properties of laser-melted deposited Ti₂Ni₃Si/NiTi intermetallic alloy, J. Alloys Compd. 465 (2008) 83–89.
- [3] X.D. Du, J.Q. Wang, G.D. Sun, D.H. Man, Effect of composition on impact-wear behavior of alloyed liner steels in corrosive condition, Mater. Sci. Eng., A 477 (2008) 277–281
- [4] H. Raghuram, C. Katsich, K. Pichelbauer, K. Koschatzky, C. Gachot, U.C. Bayr, Design of wear and corrosion resistant FeNi-graphite composites by laser cladding, Surf. Coating. Technol. 377 (2019) 124897.
- [5] G. Tranchida, M. Clesi, F. Di Franco, F. Di Quarto, M. Santamaria, Electronic properties and corrosion resistance of passive films on austenitic and duplex stainless steels, Electrochim. Acta 273 (2018) 412–423.
- [6] Q. Chen, Y.Z. Gao, Z.W. Xie, T. Chen, Y.Y. Wan, H. Wang, X. Gao, Y. Chen, Y. W. Zhou, Y.Y. Guo, Tribocorrosion behaviors of CrN coating in 3.5 wt% NaCl solution, Thin Solid Films 622 (2017) 41–47.
- [7] G. Song, Z.Q. Sun, J.D. Poplawsky, Y.F. Gao, P.K. Liaw, Microstructural evolution of single Ni₂TiAl or hierarchical NiAl/Ni₂TiAl precipitates in Fe-Ni-Al-Cr-Ti ferritic alloys during thermal treatment for elevated-temperature applications, Acta Mater. 127 (2017) 1–16.
- [8] L.J. Zheng, F.X. Zhang, R.G. Ding, F.F. Wang, H. Zhang, New phase and deformation behavior in directional solidified NiTiAl based intermetallic alloy upon cyclic tensile loading-unloading, Mater. Des. 110 (2016) 494–502.
- [9] M. Yamaguchi, H. Inui, K. Ito, High-temperature structural intermetallics, Acta Mater. 48 (2000) 307–322.
- [10] J. Zhang, X. Su, E. Strom, Z.Y. Zhong, C.H. Li, Effects of minor addition of Ni on hot-deformation behavior of gamma TiAl alloy, Mater. Sci. Eng., A 329–331 (2002) 499–503
- [11] P.R. Strutt, R.S. Polvani, J.C. Ingram, Creep behavior of the heusler type structure alloy Ni-AlTi. Metall. Trans. A 7 (1976) 23–31.
- [12] R.X. Hu, P. Nash, Q. Chen, Enthalpy of formation in the Al-Ni-Ti system, J. Phase Equilibria Diffus. 30 (2009) 559–563.
- [13] A.S. Jabur, J.T. Al-Haidary, E.S. Al-Hasani, Characterization of Ni-Ti shape memory alloys prepared by powder metallurgy, J. Alloys Compd. 578 (2013) 136–142.
- [14] H. Sina, K.B. Surreddi, S. Iyengar, Phase evolution during the reactive sintering of ternary Al-Ni-Ti powder compacts. J. Alloys Compd. 661 (2016) 294–305.
- [15] A. Dębski, W. Gąsior, A. Sypień, A. Góral, Enthalpy of formation of intermetallic phases from Al-Ni and Al-Ni-Ti systems, Intermetallics 42 (2013) 92–98.
- [16] J.C. Schuster, Z. Pan, S.H. Liu, F. Weitzer, Y. Du, On the constitution of ternary system Al-Ni-Ti, Intermetallics 15 (2007) 1257–1267.
- [17] V. Raghavan, Al-Ni-Ti (aluminum-nickel-titanium), J. Phase Equilibria Diffus. 30 (2009) 77–78.
- [18] G. Song, Z.Q. Sun, B. Clausen, P.K. Liaw, Microstructural characteristics of a Ni₂TiAl-precipitate-strengthened ferritic alloy, J. Alloys Compd. 693 (2017) 921–928.

- [19] C.H. Liebscher, V.R. Radmilović, U. Dahmen, N.Q. Vo, D.C. Dunand, M. Asta, G. Ghosh, A hierarchical microstructure due to chemical ordering in the bcc lattice: early stages of formation in a ferritic Fe-Al-Cr-Ni-Ti alloy, Acta Mater. 92 (2015) 220–232
- [20] Y.X. Yin, H.M. Wang, High-temperature wear behaviors of a laser melted Cu_{ss}/ (Cr₅Si₃-CrSi) metal silicide alloy, Mater. Sci. Eng., A 452–453 (2007) 746–750.
- [21] S. Momeni, W. Tillmann, Influence of Ag on antibacterial performance, microstructure and phase transformation of NiTi shape memory alloy coatings, Vacuum 164 (2019) 242–245.
- [22] Y. Koizumi, Y. Ro, S. Nakazawa, H. Harada, NiTi-base intermetallic alioys strengthened by Al substitution, Mater. Sci. Eng., A 223 (1997) 36–41.
- [23] S. Huang, Y. Gao, K. An, L. Zheng, W. Wu, Z. Teng, P.K. Liaw, Deformation mechanisms in a precipitation-strengthened ferritic superalloy revealed by in situ neutron diffraction studies at elevated temperatures, Acta Mater. 83 (2015) 137–148.
- [24] P. Warren, Y. Murakami, H. Harada, Phase separation in NiTi-Ni₂TiAl alloy system, Mater. Sci. Eng., A 223 (1997) 17–20.
- [25] J. Witkowska, J. Kamiński, T. Płociński, M. Tarnowski, T. Wierzchoń, Corrosion resistance of NiTi shape memory alloy after hybrid surface treatment using lowtemperature plasma, Vacuum 137 (2017) 92–96.
- [26] M. Farvizi, T. Ebadzadeh, M.R. Vaezi, E.Y. Yoon, Y.J. Kim, J.Y. Kang, H.S. Kim, A. Simchi, Effect of starting materials on the wear performance of NiTi-based composites, Wear 334–335 (2015) 35–43.
- [27] L.J. Meng, Y. Li, X.Q. Zhao, J. Xu, H.B. Xu, The mechanical properties of intermetallic Ni_{50-x}Ti₅₀-Al_x alloys (x = 6, 7, 8, 9), Intermetallics 15 (2007) 814–818.
- [28] G.W. Zhao, J. Chen, C. Ding, D. Fang, C.H. Huang, X.C. Ye, Effect of Yttrium on the microstructure, phase transformation and superelasticity of a Ti-Ni-Cu shape memory alloy, Vacuum 177 (2020) 109381.
- [29] Z.W. Xie, T. Chen, Q. Chen, Q. Yang, S. Tan, Y.J. Wang, Y.M. Luo, Z.Z. Luo, M. Q. Hua, Tribocorrosion behaviors of AlN/MoS₂-phenolic resin duplex coatings on nitrogen implanted magnesium alloys, Surf. Coating, Technol. 266 (2015) 64–69.
- [30] L. Yuan, H.M. Wang, Corrosion properties of a Cr₁₃Ni₅Si₂-based metal silicide alloy, Intermetallics 16 (2008) 1149–1155.

- [31] G. Greczynski, L. Hultman, X-ray photoelectron spectroscopy: towards reliable binding energy referencing, Prog. Mater. Sci. 107 (2020) 100591.
- [32] J. Xu, L.L. Liu, P. Munroe, Z.H. Xie, Z.T. Liang, The nature and role of passive films in controlling the corrosion resistance of MoSi₂-based nanocomposite coatings, J. Mater. Chem. 1 (2013) 10281–10291.
- [33] Q. Chen, Z.W. Xie, T. Chen, F. Gong, Tribocorrosion failure mechanism of TiN/SiO_x duplex coating deposited on AISI304 stainless steel, Materials 9 (2016) 963–975.
- [34] T.S.R.Ch Murthy, B. Basu, A. Srivastava, R. Balasubramaniam, A.K. Suri, Tribological properties of TiB₂ and TiB₂-MoSi₂ ceramic composites, J. Eur. Ceram. Soc. 26 (2006) 1293–1300.
- [35] P. Ponthiaux, F. Wenger, D. Drees, J.P. Celis, Electrochemical techniques for studying tribocorrosion processes, Wear 256 (2004) 459–468.
- [36] M.T. Mathew, T. Uth, N.J. Hallab, R. Pourzal, A. Fischer, M.A. Wimmer, Construction of a tribocorrosion test apparatus for the hip joint: Validation, test methodology and analysis, Wear 271 (2011) 2651–2659.
- [37] F.L. Ma, J.L. Li, Z.X. Zeng, Y.M. Gao, Structural, mechanical and tribocorrosion behaviour in artificial seawater of CrN/AlN nano-multilayer coatings on F690 steel substrates, Appl. Surf. Sci. 428 (2018) 404–414.
- [38] L.C. Lucas, R.A. Buchanan, J.E. Lemons, Investigations on the galvanic corrosion of multialloy total hip prostheses, J. Biomed. Mater. Res. 15 (1981) 731–747.
- [39] S.W. Watson, F.J. Friedersdorf, B.W. Madsen, S.D. Cramer, Methods of measuring wear-corrosion synergism, Wear 181 (1995) 476–484.
- [40] F. Pougoum, J.C. Qian, L. Martinu, J. Klemberg-Sapieha, Z.F. Zhou, K.Y. Li, S. Savoie, R. Lacasse, E. Potvin, R. Schulz, Study of corrosion and tribocorrosion of Fe₃Al-based duplex PVD/HVOF coatings against alumina in NaCl solution, Surf. Coating, Technol. 357 (2019) 774–783.
- [41] D. Landolt, S. Mischler, M. Stemp, Electrochemical methods in tribocorrosion: a critical appraisal, Electrochim. Acta 46 (2001) 3913–3929.
- [42] Y. Sun, E. Haruman, Effect of electrochemical potential on tribocorrosion behavior of low temperature plasma carburized 316L stainless steel in 1 M H₂SO₄ solution, Surf. Coating. Technol. 205 (2011) 4280–4290.
- [43] I. Garcia, D. Drees, J.P. Celis, Corrosion-wear of passivating materials in sliding contacts based on a concept of active wear track area, Wear 249 (2001) 452–460.